Letter

Superconductivity at carrier density 10^{17} cm^{-3} in quasi-one-dimensional $Li_{0.9}Mo_6O_{17}$

J. L. Cohn [1,*] C. A. M. dos Santos [2] and J. J. Neumeier [3]

[1]*Department of Physics, University of Miami, Coral Gables, Florida 33124, USA*

[2]*Escola de Engenharia de Lorena–University of São Paulo, Lorena, São Paulo 12602-810, Brazil*

[3]*Department of Physics, Montana State University, Bozeman, Montana 59717, USA*

(Received 8 December 2021; revised 13 August 2023; accepted 15 September 2023; published 29 September 2023)

Quasi-one-dimensional systems, having tendencies toward density-wave order in competition with superconductive pairing in their ground states, may give rise to unconventional superconductivity, a central theme in condensed matter physics. Partial density-wave gapping of electronic bands at the Fermi surface in such systems can yield superconductivity at very low carrier density that challenges Bardeen-Cooper-Schrieffer (BCS) theory since the pairing energy scale may approach or exceed the Fermi energy and render screening of the Coulomb interaction ineffective. Here we present low-T magnetotransport measurements on the quasi-one-dimensional conductor $Li_{0.9}Mo_6O_{17}$ showing the metallic state from which superconductivity emerges ($T_c \simeq 2$ K) to possess among the lowest known carrier densities, $\sim 10^{17}$ cm^{-3}, and a ratio of T_c to Fermi temperature within the BCS–Bose-Einstein-condensation crossover regime. A semimetallic state caused by a density-wave-induced Fermi surface reconstruction with highly anisotropic electron and hole pockets is implied. The degree of interpocket nesting appears to determine whether the extreme low-density ground state is superconducting or undergoes additional Fermi surface gapping.

DOI: 10.1103/PhysRevB.108.L100512

Electron pairing in the Bardeen-Cooper-Schrieffer (BCS) theory of superconductivity, arising from weak attractive interactions in a degenerate fermionic system, results in a superconducting transition temperature that is typically orders of magnitude smaller than the Fermi temperature, $T_c/T_F \sim 10^{-4}$. In the opposite limit of a Bose-Einstein condensate (BEC), strongly coupled fermions (composite bosons) condense into a coherent quantum state, and typically $T_c/T_F \gtrsim 0.1$ [1]. A small number of materials having $T_c/T_F \sim 0.04$–0.1 within the BCS-BEC crossover regime include high-T_c cuprates and heavy-fermion and Fe-based compounds, superconductors believed to involve spin-mediated pairing [2–4].

Quasi-one-dimensional (q1D) electron systems may harbor unconventional superconductivity within the BCS-BEC crossover regime when partial density-wave gapping of electronic bands at the Fermi surface (FS), induced by competing density-wave order, yields a metallic state with very small Fermi energy. $Li_{0.9}Mo_6O_{17}$ (lithium purple bronze, LiPB) is a transition metal oxide with q1D electronic properties. Its resistivity is metallic at high T, exhibits a minimum at 15 K $\lesssim T_{\min} \lesssim$ 30 K, and rises below $T_{\min}$ to the superconducting transition at $T_c \simeq 2$ K [5–7]. The metallic phase at $T \geqslant T_{\min}$ exhibits features [8,9] of a Tomonaga-Luttinger liquid (TLL) [10] with spin-charge separation [11–13]. The mechanisms for the upturn in the resistivity at $T < T_{\min}$ and superconductivity remain a mystery in spite of substantial experimental efforts over decades. The superconducting state is three dimensional with highly anisotropic upper critical fields (H_{c2}) consistent with its normal-state electrical anisotropy [7]. For field applied along the q1D chains, H_{c2} substantially exceeds the Pauli paramagnetic limit, motivating the proposal [7] that LiPB is a triplet superconductor [14–18].

The LiPB band structure, studied extensively via photoemission [19] and computation [11,19–22], consistently reveals two q1D, nearly degenerate electron bands crossing the Fermi energy, derived from d_{xy} orbital overlap along the zigzag Mo-O chains (crystallographic b axis). Superconductivity requires a dimensionality increase, for which the resistivity minimum is presumed to be the signature. Potential explanations include charge- or spin-density-wave (CDW or SDW) formation, a structural change [23,24], and a recent proposal involving the ordering of long-lived excitons [25,26]. Experiments rule out CDW [23,27,28] and SDW [29] order (though the latter less convincingly), and good agreement between the local-density approximation band structure and photoemission [19] for the bands near E_F is compelling evidence against the occurrence of a TLL fluctuation-induced suppression of dimensional crossover [30].

Here we report comprehensive magnetotransport measurements within the most conducting bc plane (field along a) at $T \gtrsim 0.4$ K for both superconducting (SC) and nonsuperconducting (non-SC) LiPB crystals, revealing extremely low carrier densities ($n \sim 10^{17}$ cm^{-3}) throughout the range $T \leqslant 100$ K and a rich multicarrier physics. The mobile carrier densities are among the lowest known for any superconductor [31,32], placing superconductivity of LiPB in a regime at the border between BCS and BEC. A density-wave-induced semimetallic reconstruction of the FS composed of highly anisotropic electron and hole pockets is implicated at $T \gg T_{\min}$ for both sets of samples. Competition for the ground state

*Corresponding author: jcohn@miami.edu

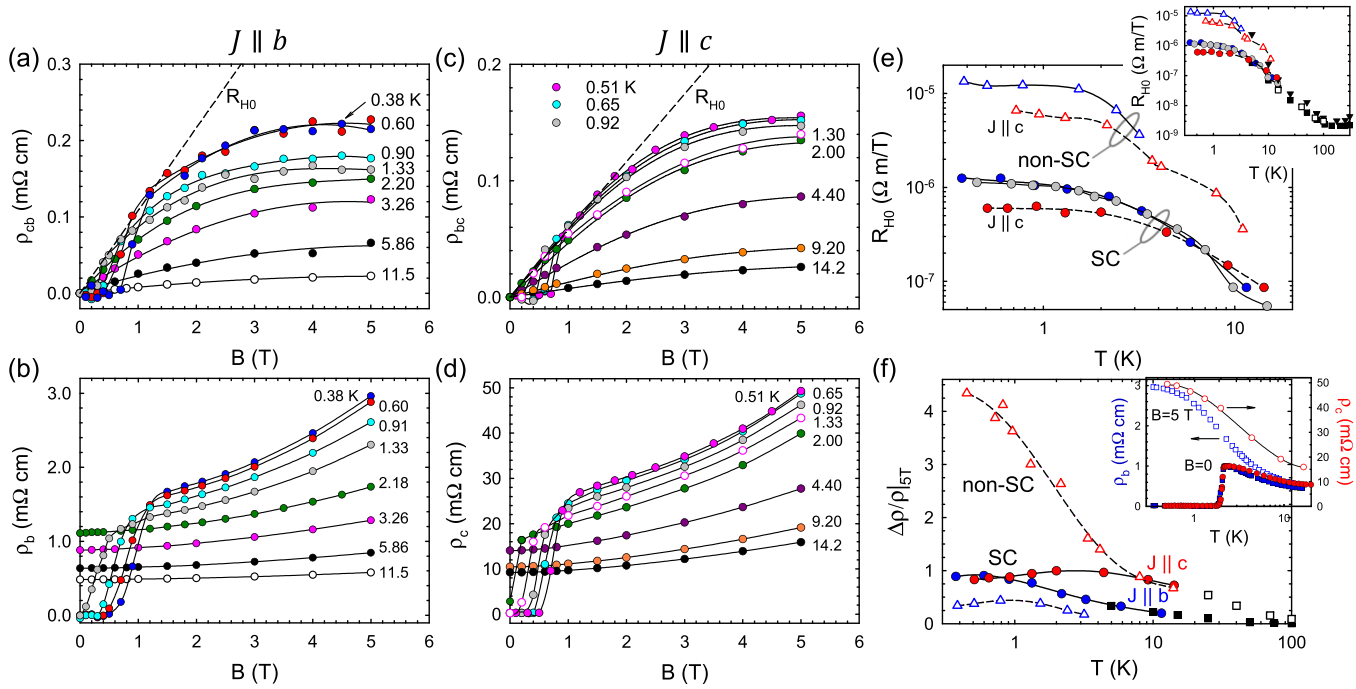

FIG. 1. (a)–(d) Hall and longitudinal resistivities for two orientations of the current flow **J** in superconducting crystals. Dashed lines in (a) and (c) are the initial slopes, $R_{H0} \equiv d\rho_{xy}/dB|_{B\to 0}$, at low T. (e) R_{H0} vs T for all crystals (SC, filled symbols; non-SC, open symbols). The inset compares data from the main panel with data at higher T for crystals from Refs. [35,36] with current parallel to b (filled squares and inverted triangles) and parallel to c (open squares). (f) Longitudinal magnetoresistance at $B = 5$ T vs T for all crystals. The inset shows $\rho_b(T)$ (squares, left ordinate) and $\rho_c(T)$ (circles, right ordinate) at $B = 0$, 5 T. Solid and dashed curves are guides for the eye.

appears to be controlled by the degree of interpocket nesting, leading to further density-wave gapping (non-SC samples) or superconductivity. This nesting is manifested in the strong scattering and localization of in-chain hole and interchain electron states on the reconstructed FS at $T \gtrsim T_{\min}$. A sharp suppression of this scattering in SC samples at $T \lesssim T_{\min}$ signals delocalization of these states and emergence of quasi-two-dimensional transport within each of the pockets as a precursor to superconductive pairing.

Figures 1(a)–1(d) show the field-dependent Hall and longitudinal resistivities for two orientations of the electric current flow ($\mathbf{J}\|b$ and $\mathbf{J}\|c$) in SC crystals at various T. Similar data for the non-SC crystals are presented in the Supplemental Material [33] (Fig. S1). Superconducting transitions are evident at low fields for temperatures $T < T_c$ [see also the inset of Fig. 1(e)]; the inferred upper critical fields and range of values for $T_{\min}$ [$\sim$18 K ($\sim$30 K) for the SC (non-SC) specimens] agree with those of prior studies [5–7] (Fig. S2 [33]).

Substantial nonlinearities of the Hall resistivities with field (especially at the lowest T) suggest the presence of charge carriers with opposing signs. The initial slopes, $R_{H0} \equiv d\rho_{xy}/dB|_{B\to 0}$ [Fig. 1(e)] yield $T \to 0$ values $R_{H0} \simeq 10^{-6}$ (10^{-5}) Ω m/T for SC (non-SC) samples, corresponding to approximate carrier densities, $n = 1/(R_{H0}e) \simeq 6 \times 10^{18}$ (6×10^{17}) cm^{-3}. However, the data are more aptly described by an anisotropic, two-carrier model, for which $R_{H0} = (n_h\mu_h^2 - n_e\mu_e^2)e/[\sigma_b(0)\sigma_c(0)]$ (where $\sigma_b(0)$ and $\sigma_c(0)$ are the zero-field conductivities) as discussed further below.

The thermoelectric coefficients tell a similar story of extremely low carrier density. The field dependencies of the Nernst signal, $N_{yx} = E_y/|\nabla T_x|$, and thermopower, $S_x = E_x/\nabla T_x$ ($x, y = b, c$), for the SC crystals are shown in Figs. 2(a)–2(d). Note the different vertical scales (millivolts versus microvolts) for N_{cb} (heat current $\mathbf{J}_q\|b$) and N_{bc} ($\mathbf{J}_q\|c$): extreme anisotropy, $N_{cb} \simeq 300N_{bc}$, is observed. Sharp maxima in the low-field Nernst signals for $T < T_c$ (especially for N_{cb}) near the midpoints of the SC transitions are attributed to a flux-flow Nernst effect [34]. Very similar results for N_{cb} were found for a second SC crystal (Fig. S3 [33]). Possible contaminating signals associated with the Righi-Leduc (thermal Hall) effect are negligible for both orientations (Fig. S4 [33]). In comparison to the Nernst signal, the thermopower is more isotropic, with a stronger field dependence evident for S_c. Though the in-chain thermopower S_b is positive, it is decidedly electronlike at $T \gtrsim 30$ K: linear in T with negative slope, resulting in negative values at $T \gtrsim 300$ K [35–37].

Like the Hall resistivity, significant nonlinearity of the Nernst signals (particularly at low T) suggests competing electron and hole contributions. For comparison with the estimates from R_{H0}, we compute carrier densities from the $B = 5$ T, $T \to 0$ limiting values for ν/T ($\nu = N/B$) and S/T indicated by the dashed lines in Figs. 2(e) and 2(f). For a broad spectrum of correlated and low-dimensional metals it has been shown [38] that these quantities scale well with carrier mobility μ and Fermi temperature T_F as prescribed by the free-electron, Boltzmann theory expressions for carrier diffusion, $\nu/T = (\pi^2/3)(k_B/e)(\mu/T_F)$ and $S/T = (\pi^2/3)(k_B/e)(1/T_F)$. Using $\mu = 0.2$ T^{-1} (determined from the analysis below) and averaging values for the two experimental orientations, $\nu/T \simeq 15$ μV/(T K^2)

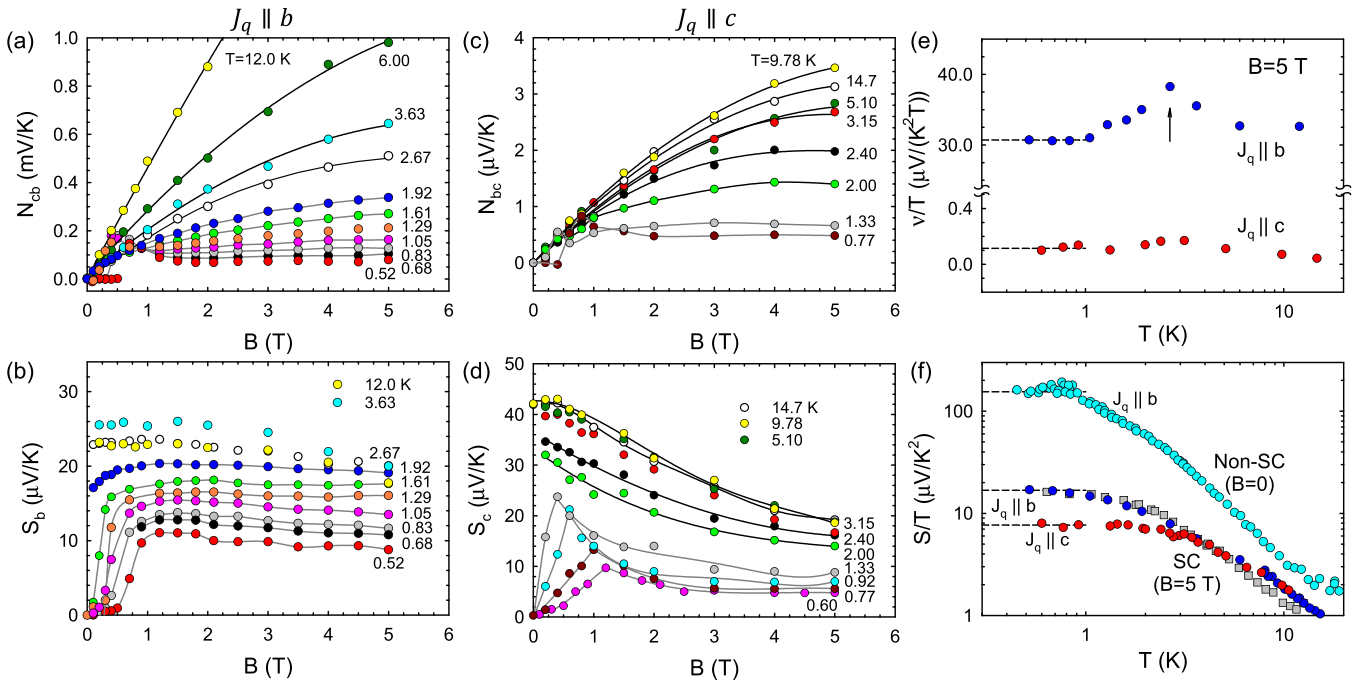

FIG. 2. (a)–(d) Nernst signal and thermopower for two orientations of the heat current $\mathbf{J}_q$ in superconducting crystals. Solid curves are guides for the eye. (e) and (f) T dependence of ν/T (e) and S/T (f). The vertical arrow in (e) marks a "kink" in ν/T near $T \simeq 3$ K (see text and Supplemental Material). The squares in (f) are from a second superconducting b-axis specimen.

($S/T \simeq 12\ \mu\text{V/K}^2$), we find $T_F \simeq 19$ K (23 K). The free-electron relation $E_F = k_B T_F = (\hbar^2/2m)(3\pi^2 n)^{2/3}$ thus implies $n \approx 3.5 \times 10^{17}\ \text{cm}^{-3}$.

To refine our understanding of the magnetotransport, consider a two-carrier model for the bc plane, with holes and electrons (densities n_h and n_e, respectively) for each direction having different mobilities, μ_{ib}, μ_{ic} ($i = h, e$) [39]. The model has four carrier densities (holes and electrons for each direction) but is simplified because for each pair of crystals (two orientations each, SC and non-SC), we observe $\rho_{cb} \simeq \rho_{bc}$ (Figs. 1(a), 1(c), and 1(e) and Supplemental Material, Fig. S1 [33]). This isotropy of the transverse magnetoresistivities contrasts with the anisotropy of the longitudinal magnetoresistivities, $\Delta\rho(B)/\rho(0)$ [Fig. 1(f)]. In such a case, the model dictates isotropy of hole and electron densities [39]. Switching to the equivalent and simpler conductivity expressions, the field dependencies of the coefficients are then given by

$$\sigma_b = \sigma_{hbb} + \sigma_{ebb} = \frac{n_h e\mu_{hb}}{(1+\mu_h^2 B^2)} + \frac{n_e e\mu_{eb}}{(1+\mu_e^2 B^2)},$$

$$\sigma_c = \sigma_{hcc} + \sigma_{ecc} = \frac{n_h e\mu_{hc}}{(1+\mu_h^2 B^2)} + \frac{n_e e\mu_{ec}}{(1+\mu_e^2 B^2)},$$

$$\sigma_{bc} = \sigma_{cb} = \sigma_{hbc} + \sigma_{ebc} = \frac{n_h e\mu_h^2 B}{(1+\mu_h^2 B^2)} - \frac{n_e e\mu_e^2 B}{(1+\mu_e^2 B^2)},$$

where $\mu_h = \sqrt{\mu_{hb}\mu_{hc}}$ and $\mu_e = \sqrt{\mu_{eb}\mu_{ec}}$ are effective mobilities governing the field dependencies. Examples of the simultaneous fitting to these equations at various temperatures and the computed partial conductivities are presented in Figs. S5–S7 [33]. The fitted values of the carrier densities and mobilities as functions of T are shown in Fig. 3. The analysis was extended to higher T for SC crystals using data from prior work [35,36] in the range $25\ \text{K} \leqslant T \leqslant 100$ K [open and filled squares in the inset of Fig. 1(e) and in Fig. 1(f)], where the magnetoresistance and Hall resistivity are quadratic and linear, respectively, in applied fields $B \leqslant 5$ T, consistent with prior studies [6,7,40,41]. The same model parameters were employed to fit the field-dependent thermoelectric coefficients (Eqs. (S1)–(S3) and Figs. S8 and S9 [33]) to extract partial coefficients for holes and electrons. The "kink" in the ν/T curve [arrow in Fig. 2(e)] is found to arise from competition between Nernst terms (carrier diffusion and the product of Hall conductivity and thermopower) with opposite sign (Eq. (S2) and Fig. S9 [33]).

A central outcome of the analysis is that, consistent with the measured $R_{H0}(T)$ for multiple specimens and orientations [inset of Fig. 1(e)], the carrier densities for both SC and non-SC crystals [Fig. 3(a)] are comparable at $T \gtrsim 10$ K, with $n_e \sim 3.5 n_h \simeq 10^{17}\ \text{cm}^{-3}$ in the former. Thus LiPB is partially compensated, with extremely low carrier densities throughout the entire T range. This result is not in conflict with established TLL physics at higher T for LiPB since TLL characteristics are independent of carrier density [42]. The single-band expression $n = 1/(R_{H0}e)$ at 100 K yields $n \sim 3 \times 10^{21}\ \text{cm}^{-3}$, a substantial overestimate of the actual value, and coincidentally comparable to, though opposite in sign, that expected from the band structure and chemical valence, 1.9 e/unit cell [13,35]. The rise in R_{H0} by more than two orders of magnitude from $T \sim 100$ K to $T \sim 10$ K [35,40,41,43] is almost entirely attributable to an increase in the effective carrier mobilities [dashed curves, Fig. 3(b)] [44].

The small density (or T_F) is incompatible with the large Fermi wave number $k_F \simeq \pi/(2b)$ determined by photoemission and density functional theory but is entirely consistent, as is compensation, with LiPB's giant Nernst coefficient over

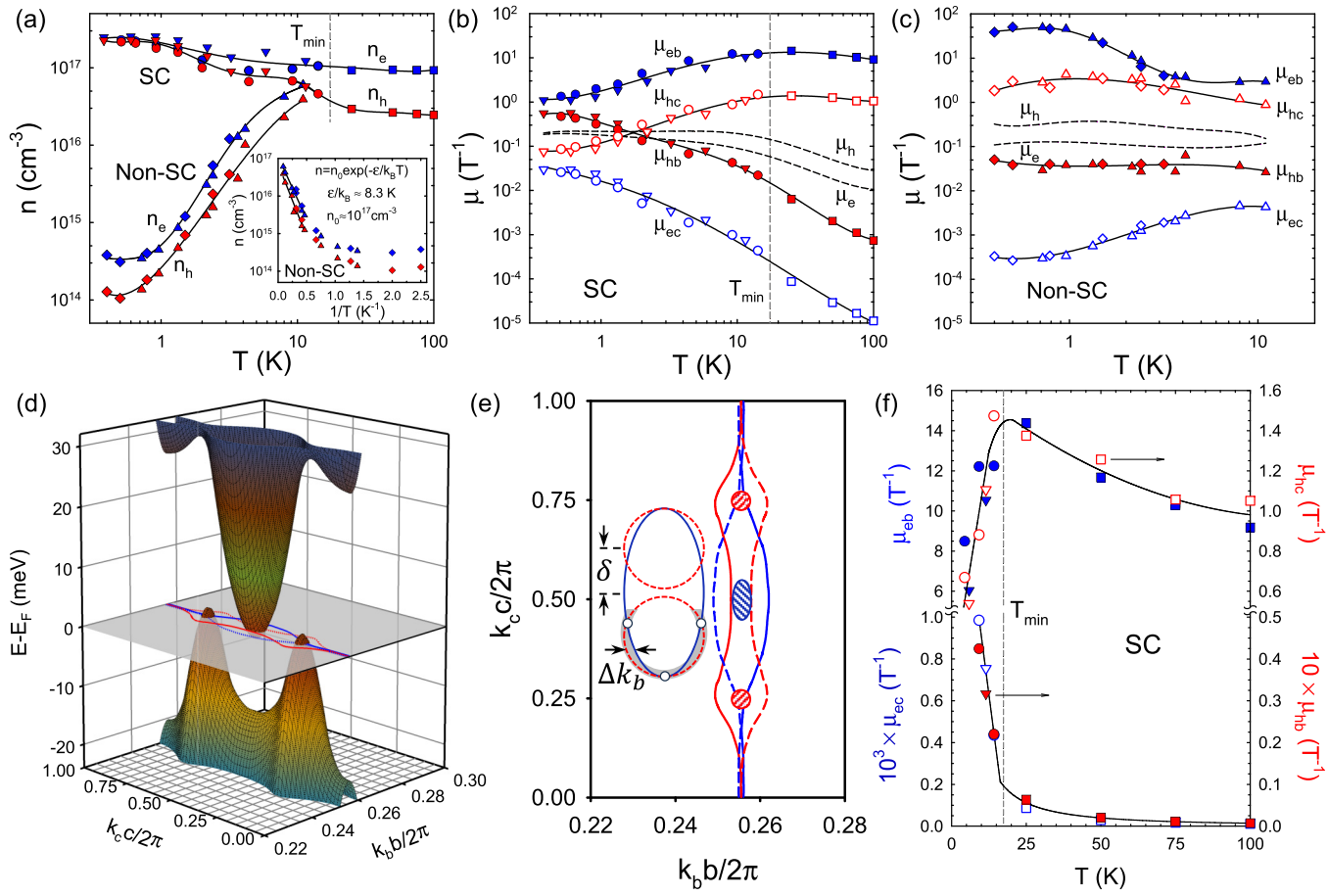

FIG. 3. Carrier densities (a) and mobilities for SC (b) and non-SC specimens (c) determined by simultaneous fitting to the anisotropic two-band model (see text and Supplemental Material). Different symbols represent the two crystals for which $\mathbf{J}\|b$ and $\mathbf{J}\|c$. Solid and dashed curves are guides for the eye. (d) Energy band scheme and Fermi plane (adapted from Ref. [19]) assuming a SDW gap-induced reconstruction to a semimetal with $E_F = 1.5$ meV for both hole and electron bands (see text). Shown in the $E = E_F$ plane of (d) and in (e) is the incomplete nesting of the unreconstructed FS (solid curves: upper sheet, red; lower sheet, blue) and their translations by the nesting vector $q_{\rm SDW} = 2k_F \simeq \pi/b$ along k_b (dashed curves), defining hole (red) and electron (blue) pockets between their respective boundaries. Note the greatly expanded scale for the k_b axis in both (d) and (e). The inset in (e) shows a magnified view of potential nesting for the electron and hole pockets (hatched regions in main panel): The best nesting is shown by the dashed hole pockets translated along k_c by $q = \pm(\pi/2c \pm \delta)$, with $\delta \sim 0.1(\pi/2c)$. The shaded region for the lower translation represents the approximate phase space at $T \approx T_{\rm min}$ for its nesting instability, the width of which normal to the FS is $\sim k_B T$ and at $T = 0$ is confined to the hot spots (small open circles). (f) Mobilities for SC samples with linear scaling (curves are guides for the eye).

a broad range of T [$\sim$45 μV/(K^2 T) at 100 K] [36]. A reconstruction of the FS (at $T > 100$ K) into small electron and hole pockets with highly anisotropic q1D character is implied. The prospect of spin-density-wave gapping of the FS for commensurate nesting vector $q_{\rm SDW} = 2k_F$ along k_b was considered in Ref. [19]. The nesting is imperfect due to small warping of the two d_{xy} FS sheets, associated with interchain (k_c) dispersions, and caused by hybridization with the gapped xz and yz valence and conduction bands via long-range indirect hopping. Gapping throughout the Brillouin zone occurs for $\Delta_{\rm SDW} \approx 65$ meV, though the interaction strength was estimated to be two to three times too small for such an instability [19]. Assuming a slightly smaller value for $\Delta_{\rm SDW}$, Fig. 3(d) depicts a semimetallic reconstruction of the bands [45] and FS using the gapped (unreconstructed) k_b (k_c) dispersions from Ref. [19] (Fig. S10 [33]). Consistent with estimates above from the thermoelectric coefficients, a small overlap was assumed with electron and hole Fermi energies being the same, $E_{F,e} = E_{F,h} = 1.5$ meV. The occupied FS areas for electrons and holes within this picture are each $\sim 3 \times 10^{-4} A_{\rm BZ}$ [$A_{\rm BZ} = (2\pi)^2/bc$ is the unreconstructed Brillouin zone area], consistent with the observed carrier densities [Fig. 3(e)]. Note the greatly expanded scale for the k_b axes in Figs. 3(d) and 3(e): The reconstructed pockets are highly anisotropic with a width along k_b of only $\sim 0.01(\pi/b)$. Within mean-field theory, the SDW transition temperature would be estimated as $T_{\rm SDW} \simeq 2\Delta_{\rm SDW}/(3.5k_B) \approx 420$ K, though incomplete nesting [46] can suppress $T_{\rm SDW}$. Alternatively, it is possible that rather than gapping large portions of the FS, strong scattering associated with density-wave fluctuations localizes states in extended, nearly nested regions of the FS sheets so that the photoemission and transport observations could be reconciled.

The overlapping electron and hole bands of the semimetallic FS reconstruction have very similar parabolic b-axis

dispersions (Fig. S10 [33]), and thus comparable values for μ_{eb} and μ_{hb} are anticipated. Indeed, for SC crystals at the lowest T ($\sim$0.4 K) this condition holds true [Fig. 3(b)]. Given that the unreconstructed band structure does not provide for in-chain hole conduction, this observation, along with the low density, provides compelling support for a semimetallic reconstruction such as that depicted in Figs. 3(d) and 3(e). However, this low-T electronic structure evolves gradually with the turning on of strong T-dependent mobilities at $T \lesssim T_{\min}$, as more clearly seen on the linear scaling of Fig. 3(f): μ_{hb} and μ_{ec} (in-chain holes and interchain electrons, lower panel) *increase* sharply below $T_{\min}$, while μ_{eb} and μ_{hc} (in-chain electrons and interchain holes, upper panel) *decrease* sharply. This opposing scattering behavior for the two groups of carriers is also reflected in opposing signs for their partial Seebeck coefficients (Fig. S8 [33]), as dictated by the scattering term in the Mott expression for diffusion thermopower, $S \sim d \ln \sigma(E)/dE|_{E_F} \sim d \ln \mu(E)/dE|_{E_F}$.

The values for μ_{hb} and μ_{ec} at $T \gtrsim 10$–20 K imply incoherence, with mean free paths that are comparable to or smaller than the interatomic spacing (Fig. S11 [33]) and three or more orders of magnitude smaller than those for in-chain electrons and interchain holes. Such highly anisotropic scattering on the FS pockets is likely associated with density-wave fluctuations and interpocket nesting for wave vectors along k_c [inset of Fig. 3(e)]. The substantial increase in the SC mobile carrier densities from $T_{\min}$ to $T \lesssim 1$ K (where they become constant), suggests that portions of the FS harbor large densities of localized states for in-chain holes and interchain electrons, the delocalization of which occurs gradually with decreasing T. This behavior may arise because the phase space for nesting [shaded region for the dashed hole FS; inset of Fig. 3(e)] declines with the thermal energy and at $T = 0$ is confined to hot spots at the intersections of the pockets (small open circles).

Supporting this picture, the in-chain hole and interchain electron states with greatest velocities lie within the shaded (nested) portions of their FSs [inset of Fig. 3(e)], while the most dispersive in-chain electron and interchain hole states remain unaffected or only partially so. Thus the decrease of the latter mobilities at $T < T_{\min}$ is a consequence of FS averaging and an increased weighting, with decreasing T, of delocalized portions of the FS having lower mobilities. Then $k_B T_{\min}$ should correspond to the maximum energy mismatch of pseudonesting, expressed approximately as $(\partial E/\partial k_b)\Delta k_b = \hbar v_{F,b} \Delta k_b$, where $v_{F,b}$ is the in-chain Fermi velocity and Δk_b is depicted in the inset of Fig. 3(e). We find $\hbar v_{F,b} \Delta k_b \simeq 0.9$ meV ($v_{F,b} = 1.8 \times 10^5$ m/s (Table S1 [33]), $E_{F,e} = E_{F,h} = 1.5$ meV as in Fig. 3(e)) and $\hbar v_{F,b} \Delta k_b \simeq 1.8$ meV ($v_{F,b} = 2.3 \times 10^5$ m/s, $E_{F,e} = 2.0$ meV, $E_{F,h} = 2.5$ meV), in reasonable accord with $k_B T_{\min}$ (1.5 meV).

A competition between further density-wave gapping of the FS and the occurrence of superconductivity will undoubtedly be sensitive to the Fermi energies of the electron and hole pockets, which presumably differ in SC and non-SC crystals. Indeed, further density-wave gapping for most of the FS is implicated in non-SC specimens by the exponential decline in carrier densities at $T \lesssim 10$ K [Fig. 3(a) and inset therein], with $n = n_0 \exp(-\varepsilon/k_B T)$ at $T \gtrsim 2$ K and averaged values $\varepsilon/k_B \simeq 8.3$ K (0.7 meV), $n_0 \simeq 10^{17}$ cm^{-3}. In spite of this carrier freeze-out, a residual density of carriers survives [$\simeq$ (1–3) $\times 10^{14}$ cm^{-3}], and the in-chain conductivity extrapolates to a finite value as $T \to 0$ (Fig. S12 [33]): Metallicity is maintained by a concomitant increase in the electron mobility μ_{eb} [Fig. 3(c)]. The high values for μ_{eb} are a consequence of a small band effective mass for the reconstructed k_b dispersions ($\sim 0.016 m_e$, Table S1 [33]) and the fact that defects in LiPB (e.g., Li vacancies or O interstitials [35]) are far from the q1D chains confining electrons and expected to interact with weak Coulomb character [22]. Further confirming this extreme low-density metallic state is the thermopower, with $\lim_{T\to 0} S_b/T \simeq 150$ μV/K [top dashed line, Fig. 2(f)]. This value is among the largest reported for any metal [47], exceeding those for strongly correlated compounds known to have substantial fractions of their FSs gapped by novel ordering [48,49]. The non-SC interchain conductivity extrapolates to zero at finite T (Supplemental Material, Fig. S12): This absence of metallicity is consistent with expectations that superconductivity is not possible in lower than two dimensions.

Comparing the non-SC mobilities with those of SC samples at the lowest T, it is notable that the values of both μ_{eb} and μ_{hc} for the former exceed those of the latter by more than an order of magnitude while the opposite is true for μ_{hb} and μ_{ec}. This is consistent with better interpocket nesting for the non-SC samples and a full gapping of these portions of the FS. The absence of this gapping in SC specimens evidently sets the stage for superconductive pairing. $T_{\min}$ effectively behaves as a dimensional crossover scale, below which the q1D electron and hole transport along mutually perpendicular directions gradually evolves to the quasi-two-dimensional character of the low-T semimetal characterized by mobile states extending in both crystallographic directions on each FS pocket.

LiPB's low carrier density is comparable to those of $SrTiO_3$ ($T_c \simeq 0.86$ K at $n = 5.5 \times 10^{17}$ cm^{-3}) [31] and pure Bi ($T_c = 0.53$ mK at $n = 3 \times 10^{17}$ cm^{-3}) [32], and thus its much higher T_c is remarkable. The interelectron distance at T_c, $d_{ee} \simeq 1/n^{1/3} \approx 22$ nm, is comparable to the relevant superconducting coherence lengths [7], $\xi_b = 30$ nm and $\xi_c = 10$ nm, i.e., Cooper pairs do not substantially overlap. This and the ratio of critical temperature to effective Fermi temperature, $T_c/T_F \gtrsim 0.1$, place LiPB's parameters near the border between BCS superconductivity and BEC [50,51]. The characteristics of LiPB revealed in this Research Letter have similarities to those of Fe-based superconductors [4] and elevate the prospect that unconventional physics is at play, e.g., spin-fluctuation-induced interpocket pairing or pairing without phase coherence at $T > T_c$ [52]. Regarding the latter, the coexistence of pairs with single-particle excitations is evidenced in LiPB [53] for specimens with partial superconducting transitions intermediate between the SC and non-SC crystals reported here.

This material is based on work supported by the U.S. DOE, Office of BES, Materials Sciences and Engineering Division, under Grants No. DE-SC0008607 (University of Miami) and No. DE-SC0016156 (Montana State University). J.L.C. acknowledges helpful comments from J. W. Allen and O. K. Andersen.

[1] M. Randeria and E. Taylor, Crossover from Bardeen-Cooper-Schrieffer to Bose-Einstein condensation and the unitary Fermi gas, Annu. Rev. Condens. Matter Phys. **5**, 209 (2014).

[2] T. Moriya and K. Ueda, Antiferromagnetic spin fluctuation and superconductivity, Rep. Prog. Phys. **66**, 1299 (2003).

[3] J. L. Sarrao and J. D. Thompson, Superconductivity in cerium- and plutonium-based '115' materials, J. Phys. Soc. Jpn. **76**, 051013 (2007).

[4] See R. M. Fernandes, A. I. Coldea, H. Ding, I. R. Fisher, P. J. Hirschfeld, and G. Kotliar, Iron pnictides and chalcogenides: a new paradigm for superconductivity, Nature (London) **601**, 35 (2022), and references therein.

[5] M. Greenblatt, W. H. McCarroll, R. Neifeld, M. Croft, and J. V. Waszczak, Quasi two-dimensional electronic properties of the lithium molybdenum bronze, $Li_{0.9}Mo_6O_{17}$, Solid State Commun. **51**, 671 (1984).

[6] X. Xu, A. F. Bangura, J. G. Analytis, J. D. Fletcher, M. M. J. French, N. Shannon, J. He, S. Zhang, D. Mandrus, R. Jin, and N. E. Hussey, Directional Field-Induced Metallization of Quasi-One-Dimensional $Li_{0.9}Mo_6O_{17}$, Phys. Rev. Lett. **102**, 206602 (2009).

[7] J.-F. Mercure, A. F. Bangura, X. Xu, N. Wakeham, A. Carrington, P. Walmsley, M. Greenblatt, and N. E. Hussey, Upper Critical Magnetic Field far above the Paramagnetic Pair-Breaking Limit of Superconducting One-Dimensional $Li_{0.9}Mo_6O_{17}$ Single Crystals, Phys. Rev. Lett. **108**, 187003 (2012).

[8] J. Hager, R. Matzdorf, J. He, R. Jin, D. Mandrus, M. A. Cazalilla, and E. W. Plummer, Non-Fermi Liquid Behavior in Quasi-One-Dimensional $Li_{0.9}Mo_6O_{17}$, Phys. Rev. Lett. **95**, 186402 (2005).

[9] F. Wang, J. V. Alvarez, S.-K. Mo, J. W. Allen, G.-H. Gweon, J. He, R. Jin, D. Mandrus, and H. Höchst, New Luttinger-Liquid Physics from Photoemission on $Li_{0.9}Mo_6O_{17}$, Phys. Rev. Lett. **96**, 196403 (2006).

[10] T. Giamarchi, *Quantum Physics in One Dimension* (Oxford University Press, Oxford, 2004).

[11] Z. S. Popović and S. Satpathy, Density-functional study of the Luttinger liquid behavior of the lithium molybdenum purple bronze $Li_{0.9}Mo_6O_{17}$, Phys. Rev. B **74**, 045117 (2006).

[12] P. Chudzinski, T. Jarlborg, and T. Giamarchi, Luttinger-liquid theory of purple bronze $Li_{0.9}Mo_6O_{17}$ in the charge regime, Phys. Rev. B **86**, 075147 (2012).

[13] J. Merino and R. H. McKenzie, Effective Hamiltonian for the electronic properties of the quasi-one-dimensional material $Li_{0.9}Mo_6O_{17}$, Phys. Rev. B **85**, 235128 (2012).

[14] A. G. Lebed and O. Sepper, Possible triplet superconductivity in the quasi-one-dimensional conductor $Li_{0.9}Mo_6O_{17}$, Phys. Rev. B **87**, 100511(R) (2013).

[15] O. Sepper and A. G. Lebed, Nodeless versus nodal scenarios of possible triplet superconductivity in the quasi-one-dimensional layered conductor $Li_{0.9}Mo_6O_{17}$, Phys. Rev. B **88**, 094520 (2013).

[16] W. Cho, C. Platt, R. H. McKenzie, and S. Raghu, Spin-triplet superconductivity in a weak-coupling Hubbard model for the quasi-one-dimensional compound $Li_{0.9}Mo_6O_{17}$, Phys. Rev. B **92**, 134514 (2015).

[17] N. Lera and J. V. Alvarez, Triplet superconductivity in a model of $Li_{0.9}Mo_6O_{17}$, Phys. Rev. B **92**, 174523 (2015).

[18] C. Platt, W. Cho, R. H. McKenzie, R. Thomale, and S. Raghu, Spin-orbit coupling and odd-parity superconductivity in the quasi-one-dimensional compound $Li_{0.9}Mo_6O_{17}$, Phys. Rev. B **93**, 214515 (2016).

[19] L. Dudy, J. W. Allen, J. D. Denlinger, J. He, M. Greenblatt, M. W. Haverkort, Y. Nohara, and O. K. Andersen, Wannier-orbital theory and ARPES for the quasi-1D conductor $LiMo_6O_{17}$, arXiv:1812.03388.

[20] M. H. Whangbo and E. Canadell, Band electronic structure of the lithium molybdenum purple bronze $Li_{0.9}Mo_6O_{17}$, J. Am. Chem. Soc. **110**, 358 (1988).

[21] M. Nuss and M. Aichhorn, Effective model for the electronic properties of quasi-one-dimensional purple bronze $Li_{0.9}Mo_6O_{17}$ based on *ab initio* calculations, Phys. Rev. B **89**, 045125 (2014).

[22] T. Jarlborg, P. Chudzinski, and T. Giamarchi, Effects of thermal and spin fluctuations on the band structure of purple bronze $Li_2Mo_{12}O_{34}$, Phys. Rev. B **85**, 235108 (2012).

[23] C. A. M. dos Santos, B. D. White, Y.-K. Yu, J. J. Neumeier, and J. A. Souza, Dimensional Crossover in the Purple Bronze $Li_{0.9}Mo_6O_{17}$, Phys. Rev. Lett. **98**, 266405 (2007).

[24] M. S. da Luz, J. J. Neumeier, C. A. M. dos Santos, B. D. White, H. J. Izario Filho, J. B. Leao, and Q. Huang, Neutron diffraction study of quasi-one-dimensional lithium purple bronze: Possible mechanism for dimensional crossover, Phys. Rev. B **84**, 014108 (2011).

[25] P. Chudzinski, Multi-orbital physics in lithium-molybdenum purple-bronze: Going beyond paradigm, Eur. Phys. J. B **90**, 148 (2017).

[26] J. Lu, X. Xu, M. Greenblatt, R. Jin, P. Tinnemans, S. Licciardello, M. R. van Delft, J. Buhot, P. Chudzinski, and N. E. Hussey, Emergence of a real-space symmetry axis in the magnetoresistance of the one-dimensional conductor $Li_{0.9}Mo_6O_{17}$, Sci. Adv. **5**, eaar8027 (2019).

[27] J. Choi, J. L. Musfeldt, J. He, R. Jin, J. R. Thompson, D. Mandrus, X. N. Lin, V. A. Bondarenko, and J. W. Brill, Probing localization effects in $Li_{0.9}Mo_6O_{17}$ purple bronze: An optical-properties investigation, Phys. Rev. B **69**, 085120 (2004).

[28] G. Wu, X.-s. Ye, X. Zeng, B. Wu, and W. G. Clark, Direct observation of charge state in the quasi-one-dimensional conductor $Li_{0.9}Mo_6O_{17}$, Sci. Rep. **6**, 20721 (2016).

[29] J. Chakhalian, Z. Salman, J. Brewer, A. Froese, J. He, D. Mandrus, and R. Jin, Magnetism in purple bronze $Li_{0.9}Mo_6O_{17}$, Phys. B (Amsterdam) **359-361**, 1333 (2005).

[30] D. Boies, C. Bourbonnais, and A.-M. S. Tremblay, One-Particle and Two-Particle Instability of Coupled Luttinger Liquids, Phys. Rev. Lett. **74**, 968 (1995).

[31] X. Lin, Z. Zhu, B. Fauqué, and K. Behnia, Fermi Surface of the Most Dilute Superconductor, Phys. Rev. X **3**, 021002 (2013).

[32] O. Prakash, A. Kumar, A. Thamizhavel, and S. Ramakrishnan, Evidence for bulk superconductivity in pure bismuth single crystals at ambient pressure, Science **355**, 898 (2017).

[33] See Supplemental Material at http://link.aps.org/supplemental/10.1103/PhysRevB.108.L100512 for additional experimental details, data, and analysis. It includes Ref. [54].

[34] K. Behnia, Nernst response, viscosity and mobile entropy in vortex liquids, J. Phys.: Condens. Matter **35**, 074003 (2023).

[35] J. L. Cohn, P. Boynton, J. S. Triviño, J. Trastoy, B. D. White, C. A. M. dos Santos, and J. J. Neumeier, Stoichiometry, structure,

and transport in the quasi-one-dimensional metal $Li_{0.9}Mo_6O_{17}$, Phys. Rev. B **86**, 195143 (2012).

[36] J. L. Cohn, B. D. White, C. A. M. dos Santos, and J. J. Neumeier, Giant Nernst Effect and Bipolarity in the Quasi-One-Dimensional Metal $Li_{0.9}Mo_6O_{17}$, Phys. Rev. Lett. **108**, 056604 (2012).

[37] J. L. Cohn, S. Moshfeghyeganeh, C. A. M. dos Santos, and J. J. Neumeier, Extreme Thermopower Anisotropy and Interchain Transport in the Quasi-One-Dimensional Metal $Li_{0.9}Mo_6O_{17}$, Phys. Rev. Lett. **112**, 186602 (2014).

[38] K. Behnia, The Nernst effect and the boundaries of the Fermi liquid picture, J. Phys.: Condens. Matter **21**, 113101 (2009).

[39] Q. Deng, J. Xing, J. Liu, H. Yang, and H.-Hu. Wen, Anisotropic electronic mobilities in the nematic state of the parent phase NaFeAs, Phys. Rev. B **92**, 014510 (2015).

[40] H. Chen, J. J. Ying, Y. L. Xie, G. Wu, T. Wu, and X. H. Chen, Magnetotransport properties in purple bronze $Li_{0.9}Mo_6O_{17}$ single crystal, Europhys. Lett. **89**, 67010 (2010).

[41] N. Wakeham, A. F. Bangura, X. Xu, J.-F. Mercure, M. Greenblatt, and N. E. Hussey, Gross violation of the Wiedemann–Franz law in a quasi-one-dimensional conductor, Nat. Commun. **2**, 396 (2011).

[42] S. Wang, F. Wu, S. Zhao, K. Watanabe, T. Taniguchi, C. Zhou, and F. Wang, Logarithm diameter scaling and carrier density independence of one-dimensional Luttinger liquid plasmon, Nano Lett. **19**, 2360 (2019).

[43] J. Dumas and C. Schlenker, Charge density wave properties of molybdenum bronzes, Int. J. Mod. Phys. B **07**, 4045 (1993).

[44] Contrary to the case for a single band, the mobilities do not cancel in the Hall expression even when momentum independent, $R_{H0} \simeq \frac{1}{B}\frac{\sigma_{bc}}{\sigma_b\sigma_c} \simeq \frac{1}{n_e e}\frac{\mu_{hb}}{\mu_{eb}} - \frac{1}{n_h e}\frac{\mu_{ec}}{\mu_{hc}}$, valid for most of the T range where $\mu_{eb} \gg \mu_{hb}$ and $\mu_{hc} \gg \mu_{ec}$.

[45] The approximate energy band scheme depicted in Fig. 3(d) employs the k_c dispersions at a single value $k_b(b/2\pi) = 0.25$ from Fig. 12 of Ref. [19]: It does not incorporate changes in the dispersions with energy. For the very small Fermi energies depicted, this should have little effect on the shape of the electron and hole pockets of the reconstructed FS. See Supplemental Material for additional details.

[46] X. Huang and K. Maki, Imperfect nesting in spin-density waves, Phys. Rev. B **46**, 7219 (1992).

[47] K. Behnia, D. Jaccard, and J. Flouquet, On the thermoelectricity of correlated electrons in the zero-temperature limit, J. Phys. (Amsterdam) **16**, 5187 (2004).

[48] A. Hiess, C. Geibel, G. Sparn, C. D. Bredl, F. Steglich, T. Takabatake, and H. Fujii, Transport properties of CeNiSn at low temperatures and in high magnetic fields, Phys. B (Amsterdam) **199-200**, 437 (1994).

[49] A. Pourret, K. Behnia, D. Kikuchi, Y. Aoki, H. Sugawara, and H. Sato, A. Pourret, K. Behnia, D. Kikuchi, Y. Aoki, H. Sugawara, and H. Sato, Drastic Change in Transport of Entropy with Quadrupolar Ordering in $PrFe_4P_{12}$, Phys. Rev. Lett. **96**, 176402 (2006).

[50] Y. J. Uemura, Classifying superconductors in a plot of T_c versus Fermi temperature T_F, Phys. C (Amsterdam) **185-189**, 733 (1991).

[51] A. Pourret, L. Malone, A. B. Antunes, C. S. Yadav, P. L. Paulose, B. Fauqué, and K. Behnia, Strong correlation and low carrier density in $Fe_{1+y}Te_{0.6}Se_{0.4}$ as seen from its thermoelectric response, Phys. Rev. B **83**, 245117(R) (2011).

[52] A. V. Chubukov, I. Eremin, and D. V. Efremov, Superconductivity versus bound-state formation in a two-band superconductor with small Fermi energy: Applications to Fe pnictides/chalcogenides and doped $SrTiO_3$, Phys. Rev. B **93**, 174516 (2016).

[53] C. A. M. dos Santos, M. S. da Luz, Y.-K. Yu, J. J. Neumeier, J. Moreno, and B. D. White, Electrical transport in single-crystalline $Li_{0.9}Mo_6O_{17}$: A two-band Luttinger liquid exhibiting Bose metal behavior, Phys. Rev. B **77**, 193106 (2008).

[54] W. H. McCarroll and M. Greenblatt, Preparation of lithium molybdenum oxide bronzes by a temperature gradient flux growth technique, J. Solid State Chem. **54**, 282 (1984).

Supplemental Material for:

"Superconductivity at carrier density 10^{17}cm^{-3} in quasi-one-dimensional $Li_{0.9}Mo_6O_{17}$"

J. L. Cohn, C. A. M. dos Santos, and J. J. Neumeier

Experimental methods

$Li_{0.9}Mo_6O_{17}$ crystal growth [23, 54] and crystallographic and stoichiometric studies [24, 35] on similarly-grown crystals have been reported previously. It is common to find superconducting (SC) and non-superconducting (non-SC) single crystals in the same growth vessel, indicating slight stoichiometric variations that occur naturally during the growth process. All measurements were performed with applied field normal to the *bc*-plane (we ignore the small angle $\sim 0.6°$ between field and *a* axis of the monoclinic unit cell).

Specimens were oriented by x-ray diffraction and polished into thin parallelepipeds with typical dimensions 0.05-0.15 mm along *a* and 0.5-2 mm in the *b*-*c* plane. A six-contact geometry using sputter-deposited Au contacts and two-thermometer, one-heater method was employed for the electric and thermoelectric measurements. The polished, cut, and oriented crystals were cleaned ultrasonically prior to sputter deposition of gold contacts on both sides of the crystal. This ensured some gold deposition on the thin side edges as well, thereby creating ring-like contacts with shorting along the *a* axis. Gold wires (0.001" diameter) were bonded to the contacts with silver epoxy. A matched pair of RuO sensors, mounted on thin OFC Cu plates were suspended in vacuum and thermally linked to the specimens with 0.005"-diameter gold wires, the ends of which were bonded to the Cu plates and to the specimen (along the crystal width atop the gold longitudinal voltage contacts) with silver epoxy.

During field sweeps the field was stabilized at each setting. The dc longitudinal and Hall resistivities were determined with both current and field reversal. With the heater energized, the thermopower and Nernst voltages were determined from the symmetric and antisymmetric combinations of the longitudinal and transverse voltages, respectively, measured for both field orientations.

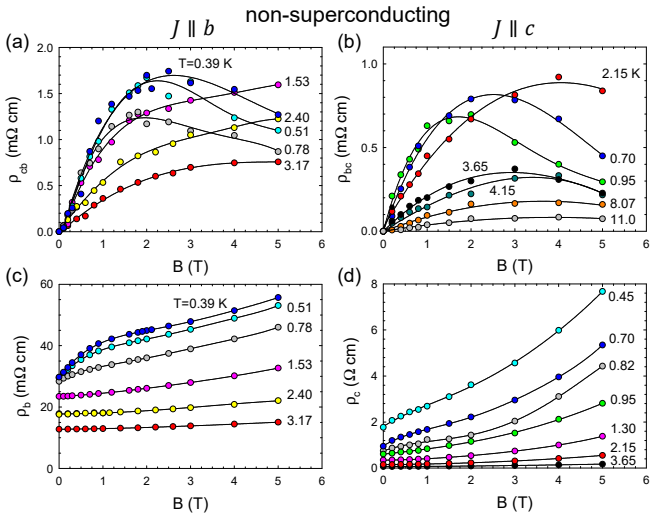

Fig. S1. Hall and longitudinal resistivities for two orientations of the current flow (**J**||**b** and **J**||**c**) in non-superconducting crystals. Solid curves are guides.

Additional data

Figure S1 shows the field-dependent Hall and longitudinal resistivities for two orientations of the current flow (**J**||**b** and **J**||**c**) for non-superconducting crystals at various temperatures. A decrease in the longitudinal resistivity (but absence of a zero-resistance state) evident at the lowest temperatures and fields, suggests partial, inhomogeneous

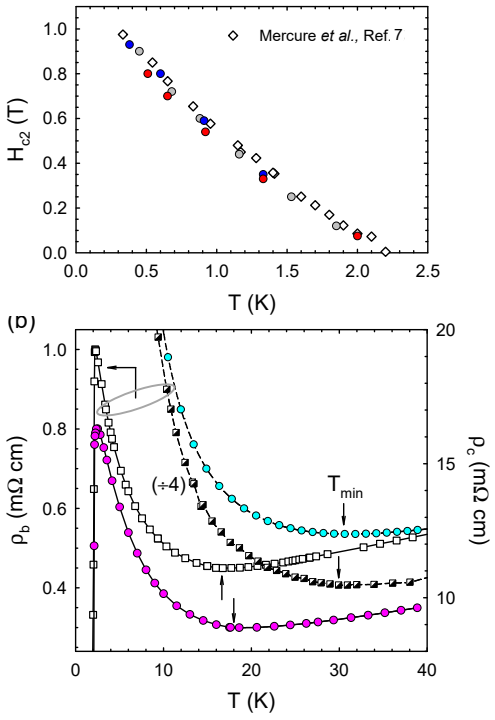

Fig. S2. (a) Upper critical fields $H_{c2}(T)$ for three superconducting crystals [same filled symbols as in Fig. 1 (e), (f)] compared with data from Ref. 7 (open symbols). (b) Resistivity data showing values for T_{min} (arrows) for the superconducting (solid curves) and non-superconducting (dashed curves) crystals in the main text for current along the *b* and *c* axes (squares–left ordinate, circles–right ordinate, respectively). The ρ_b data for the non-superconducting crystal are divided by 4.

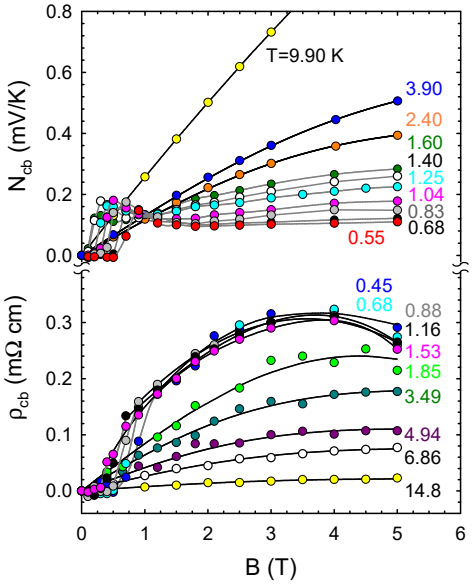

Fig. S3. Field dependence of the Nernst signal (upper panel) and Hall resistivity (lower panel) for a second crystal with current along the chains (cystallographic b axis). Solid curves are guides.

superconductivity, similar to that observed in prior studies [53].

Figure S2 (a) shows the upper critical fields (determined using a 50% resistance criterion) for three superconducting specimens (filled symbols) in comparison to data from Mercure *et al.* [7] for this field orientation. The zero-field resistivities for the superconducting and non-superconducting crystals are shown in Fig. S2 (b) where values for T_{min} are seen to be ~ 18 K and 30 K, respectively.

Figure S3 shows the field dependence of the Nernst signal (upper panel) and Hall resistivity (lower panel) for a second superconducting crystal with electric and heat currents along the Mo-O chains (crystallographic b axis).

Possible contamination of thermoelectric signals due to a Righi-Leduc transverse temperature difference

The Nernst expressions (derived in the next section) assume the presence of no thermal gradients other than those along the primary heat flow directions. A slight misalignment of the crystallographic and body axes can mix the signals from the orthogonal crystallographic axes, but these cross-contaminations are eliminated upon computing the appropriate field-symmetrized and antisymmetrized combinations. A potential intrinsic source of a transverse temperature gradient is the Righi-Leduc (thermal Hall) effect [41]. For a specimen with primary heat flow along the c axis, a Righi-Leduc-induced ΔT_b can generate two contaminating signals: (1) a transverse thermopower voltage in response to ΔT_b, $V_{bc} = S_{bb}\Delta T_b$ and (2) a Nernst voltage along the primary thermal gradient, $V_{cc} = (w/\ell)N_{cb}\Delta T_b$ (w is the transverse specimen dimension and ℓ the longitudinal distance between electrical contacts). As the Righi-Leduc ΔT_b is an odd function of the applied field, signal (1) will be odd in field and potentially contaminate the transverse Nernst signal (N_{bc}) induced by the fixed primary ΔT_c. Since the Nernst voltage is itself odd in field, signal (2) will be even in field and potentially contaminate the thermopower (S_{cc}) signal.

The Righi-Leduc-induced temperature difference is given by,

$$\Delta T_b = \left(\frac{w}{\ell}\right)\frac{\kappa_{bc}}{\kappa_{bb}}\Delta T_c.$$

Substituting this in the expression for the potential contaminating signal V_{bc} above and adding to it the expected Nernst signal from the primary gradient gives $V_{bc} \propto S_{bb}(\kappa_{bc}/\kappa_{bb}) + N_{bc}$. The results from Ref. 41 suggest $\kappa_{bc}/\kappa_{bb} \gtrsim 0.5$ at $T = 25$ K. But it is clear from Fig. 2 (c) that S_{bb} is only weakly field dependent in the normal state and remains finite at $B = 0$ – the contaminating signal would introduce a step-like change in sign in the measured V_{bc} if it is of significant magnitude in comparison to the Nernst term. Figure S4 shows the raw transverse thermoelectric signal for this configuration at $T = 9.78$ K and 2.00 K – no such discontinuities are observed and the signals pass smoothly through the origin at $B = 0$. For comparison we used the S_{bb} data at $T = 12$ K to simulate the effect of a contaminating signal on the $T = 9.78$ K Nernst data, assuming a much smaller $\kappa_{bc}/\kappa_{bb} = 0.03$ (×'s in Fig. S4). This yields a ΔT_b that is $\sim 1\%$ of the primary ΔT_c for this specimen, i.e. $\lesssim 1-2$ mK throughout the T range. Accordingly, we can also conclude that potential contaminating signal (2) above is negligible in comparison to the longitudinal thermopower voltage. These arguments also apply for the other orientation (primary heat flow along the b axis) where the Nernst signal is substantially larger and the relevant thermopower (S_{cc}) for contaminating signal (1) is of comparable magnitude.

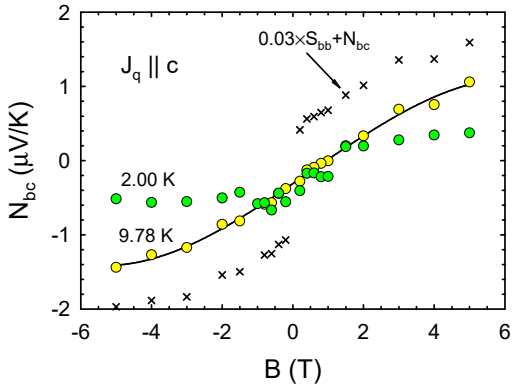

Fig. S4. Field dependence of the raw Nernst signal for the c-axis superconducting specimen ($\mathbf{J_q}\|\mathbf{c}$) at $T = 9.78$ K and 2.00 K before multiplying by $\ell/w = 3.15$ [the field-antisymmetrized data is shown in Fig. 2 (b)]. Also shown (×) are the Nernst data at 9.78 K with the addition of a small contaminating signal from the b-axis thermopower driven by a hypothetical Righi-Leduc transverse ΔT_b as discussed in the text.

The absence of a significant transverse temperature difference in our measurements is not in conflict with the results of Ref. 41 given that the Au wire heat links spanning the crystal width on the longitudinal voltage contacts in the present experiments will tend to suppress a transverse temperature difference across the Hall contacts midway between them. Supporting this hypothesis, we estimate that at $T = 2$ K the thermal conductance of the two Au mounting wires (taking $\kappa_{Au} = 150$ W/mK) is ~ 7 times that of the specimen (using $\kappa_{LiPB} = 10$ W/mK from our direct measurements) along its transverse dimension.

Anisotropic, two-carrier transport model

As noted in the main text, we employed a two-carrier transport model with anisotropic mobilities [39] to describe transport in the *b*-*c* plane transverse to the applied magnetic field. The longitudinal and transverse conductivities as functions of applied field are then given by,

$$\sigma_b = \sigma_{hbb} + \sigma_{ebb} = \frac{n_h e\mu_{hb}}{\left(1+\mu_h^2 B^2\right)} + \frac{n_e e\mu_{eb}}{\left(1+\mu_e^2 B^2\right)}$$
$$\sigma_c = \sigma_{hcc} + \sigma_{ecc} = \frac{n_h e\mu_{hc}}{\left(1+\mu_h^2 B^2\right)} + \frac{n_e e\mu_{ec}}{\left(1+\mu_e^2 B^2\right)}$$
$$\sigma_{bc} = \sigma_{cb} = \sigma_{hbc} + \sigma_{ebc} = \frac{n_h e\mu_h^2 B}{\left(1+\mu_h^2 B^2\right)} - \frac{n_e e\mu_e^2 B}{\left(1+\mu_e^2 B^2\right)},$$

where $\mu_h = \sqrt{\mu_{hb}\mu_{hc}}$ and $\mu_e = \sqrt{\mu_{eb}\mu_{ec}}$ are the effective mobilities governing the field dependencies.

The thermopowers are sums of the partial hole and electron thermopowers (diagonal components of the Seebeck tensor $\overleftrightarrow{S}$), weighted by their conductivities:

$$S_b \equiv S_{bb} = \left(\frac{\sigma_{hbb}}{\sigma_{bb}}\right) S_{hbb} + \left(\frac{\sigma_{ebb}}{\sigma_b}\right) S_{ebb} \qquad \text{(S1)}$$
$$S_c \equiv S_{cc} = \left(\frac{\sigma_{hcc}}{\sigma_{cc}}\right) S_{hcc} + \left(\frac{\sigma_{ecc}}{\sigma_c}\right) S_{ecc}$$

The Nernst signal is given by [38],

$$N_{cb} \equiv \frac{E_c}{|\nabla T_b|} = \frac{\sigma_{bb}\alpha_{cb} - \sigma_{cb}\alpha_{bb}}{\sigma_{bb}\sigma_{cc} - \sigma_{bc}\sigma_{cb}}$$
$$N_{bc} \equiv \frac{E_b}{|\nabla T_c|} = \frac{\sigma_{cc}\alpha_{bc} - \sigma_{bc}\alpha_{cc}}{\sigma_{bb}\sigma_{cc} - \sigma_{bc}\sigma_{cb}},$$

where $\overleftrightarrow{\alpha} = \overleftrightarrow{\sigma}\cdot\overleftrightarrow{S}$ is the Peltier conductivity tensor. Expressing $\overleftrightarrow{\alpha}$ in terms of $\overleftrightarrow{\sigma}$ and $\overleftrightarrow{S}$, and dropping small terms of second order in the Hall conductivities yields:

$$N_{cb} = \frac{\sigma_{hcc}S_{hcb} + \sigma_{ecc}S_{ecb}}{\sigma_{cc}} + \frac{(\sigma_{ebb}\sigma_{hcb} - \sigma_{hbb}\sigma_{ecb})(S_{hbb} - S_{ebb})}{\sigma_{bb}\sigma_{cc}} \qquad \text{(S2)}$$
$$N_{bc} = \frac{\sigma_{hbb}S_{hbc} + \sigma_{ebb}S_{ebc}}{\sigma_{bb}} + \frac{(\sigma_{ecc}\sigma_{hbc} - \sigma_{hcc}\sigma_{ebc})(S_{hcc} - S_{ecc})}{\sigma_{bb}\sigma_{cc}}$$

The first terms reflect carrier diffusion, with the weighting of hole and electron off-diagonal thermopowers by their respective partial conductivities. The second terms reflect the contribution from the Lorentz-force deflection of longitudinal electron and hole currents of opposite polarity, driven by the Seebeck electric field ($J_{net} = 0$ for the open circuit conditions). The diagonal and off-diagonal components of the thermopower tensor have field dependencies like those of the conductivity:

$$S_{hbb} = \frac{S^0_{hbb}}{\left(1+\mu_h^2 B^2\right)}, \qquad S_{hcc} = \frac{S^0_{hcc}}{\left(1+\mu_h^2 B^2\right)} \qquad \text{(S3)}$$
$$S_{hbc} = \frac{S^0_{hbc}\mu_h B}{\left(1+\mu_h^2 B^2\right)}, \qquad S_{hcb} = \frac{S^0_{hcb}\mu_h B}{\left(1+\mu_h^2 B^2\right)}$$

where S^0_{hbb}, S^0_{hcc}, S^0_{hbc}, and S^0_{hcb} are constants and similar expressions define the B dependencies for S_{ebb}, S_{ecc}, S_{ebc}, and S_{ecb}.

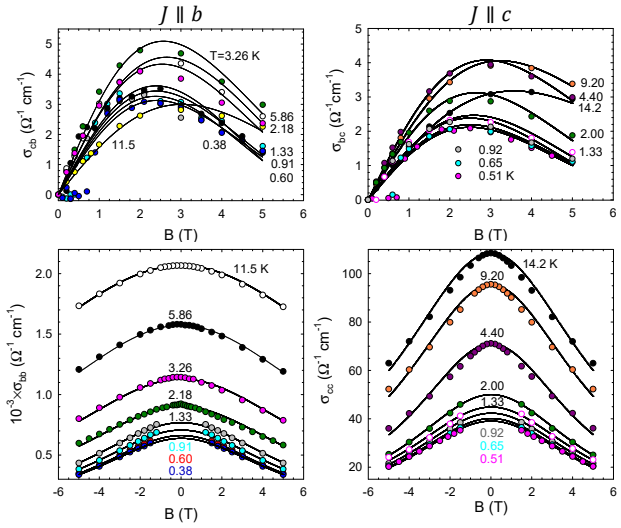

Fig. S5. Hall and longitudinal conductivities for superconducting specimens. Solid curves are generated by simultaneous fitting to the anisotropic two-carrier model with parameters shown in Fig. 3.

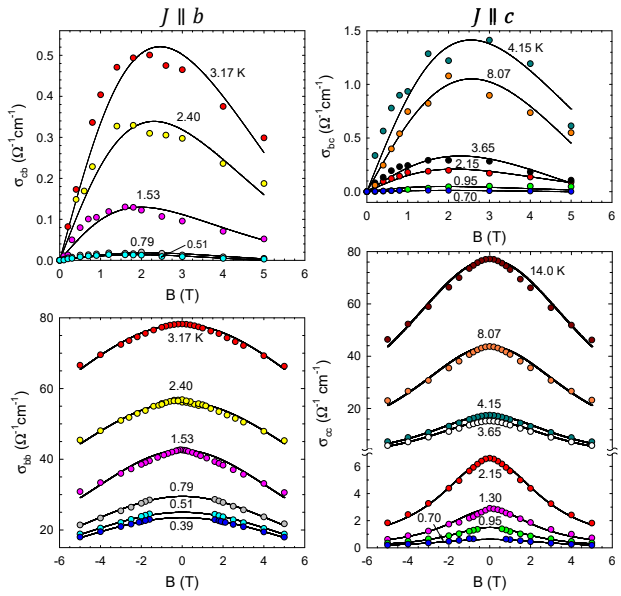

Fig. S6. Hall and longitudinal conductivities for non-superconducting specimens. Solid curves are generated by simultaneous fitting to the anisotropic two-carrier model with parameters shown in Fig. 3.

Simultaneous fitting of the Hall and longitudinal conductivities to the anisotropic two-carrier model

Fitting the model to the conductivities rather than to the more complex resistivity expressions [39] gave more reliable convergence of the fit parameters (the separate terms in the Hall conductivity each contain only two fit parameters). The Hall and longitudinal conductivities were computed from the measured tensor components of the resistivities, e.g., $\sigma_{bc} = \rho_{bc}/(\rho_{bb}\rho_{cc} + \rho_{bc}\rho_{cb}) \approx \rho_{bc}/(\rho_{bb}\rho_{cc})$ and $\sigma_{bb} = 1/\rho_{bb}$. The Hall and longitudinal conductivities for a particular current orientation were employed along with the longitudinal conductivity for the other orientation at the same temperature or interpolations in T on the data sets for the other orientation when measurements at the same temperature were unavailable. In practice the four independent fit parameters employed were μ_{hb}, μ_{eb}, and the effective mobilities $\mu_h = \sqrt{\mu_{hb}\mu_{hc}}$ and $\mu_e = \sqrt{\mu_{eb}\mu_{ec}}$, with μ_{hc} and μ_{ec} computed from these. The standard error in all fitting parameters was 15-20% throughout the temperature range. The quality of the fitting (Figs. S5 and S6) is generally very good, though the fits to $\sigma_{cc}(B)$ at $T > T_c$ are poorer, suggesting a modest field dependence of the c-axis hole mobility, μ_{hc}.

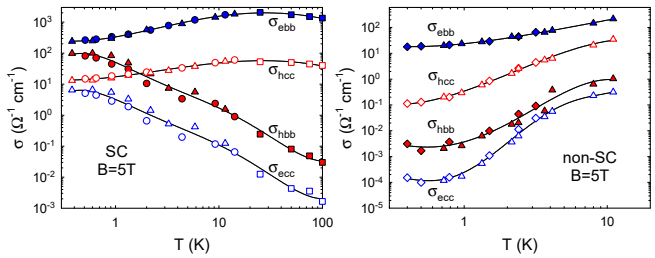

Fig. S7. Partial conductivities at $B = 5$ T computed from the anisotropic two-carrier model fitting parameters from Fig 3. Solid curves are guides.

The four partial conductivities for both SC and non-SC crystals at $B = 5$ T, computed from the fitting parameters in Fig. 3, are shown in Fig. S7.

Fitting of the thermopower and Nernst field dependencies

Using the carrier densities and mobilities determined from fitting to the magnetoconductivities, we first fitted the thermopower versus field data, treating the two partial thermopowers (TEPs) for each direction as the only adjustable parameters (Eqs. S1, S3). These partial TEPs were then employed in similar fittings of the Nernst signals versus field, introducing two additional partial (off-diagonal) TEPs for each direction as adjustable parameters (Eq. S2). We restricted the analysis to $T \lesssim 3$ K since the smaller partial conductivities (in-chain holes, interchain electrons) become too small ($\lesssim 1\%$ of the total conductivity) at higher T to give reliable results for their partial TEPs. The fitting results are represented as dashed curves in Fig. S8 (a)-(d). The resulting T-dependent partial TEPs at $B = 5$ T are shown in Fig. S8 (e). They are linear in T at $T \leq 1.3$ K (dashed lines), but with opposite signs for the two groups of carriers (in-chain electrons, interchain holes) and (in-chain holes, interchain electrons), and with $\lim_{T\to 0} |S/T|$ approximately 2.5 times larger for the latter. The opposing signs of the partial TEPs are attributable to the opposing signs of the scattering terms, $d\mu/dE \propto d\mu/dT$, in the Mott expression

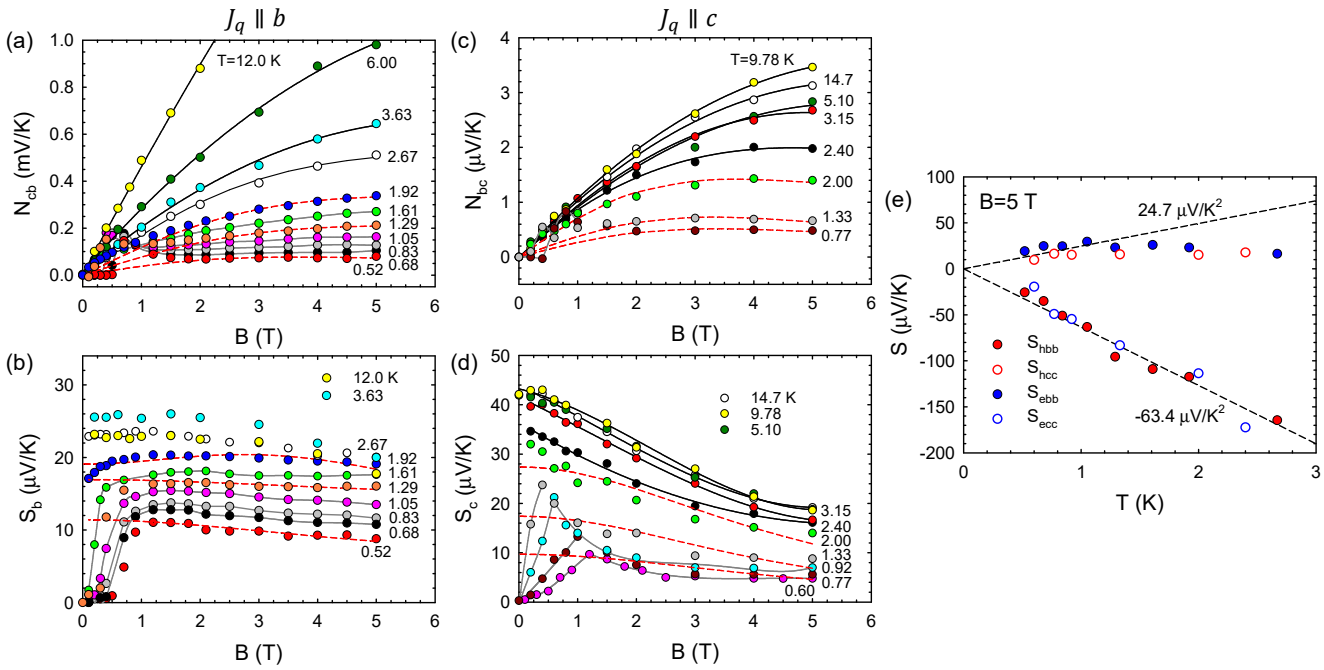

Fig. S8. (a)-(d) Nernst signal and thermopower data for SC samples reproduced from Fig. 2 with examples of fits (dashed curves) to the anisotropic two-carrier model at three temperatures for each orientation (Eqs. S1, S3). (e) $B = 5T$ partial thermopowers determined from the same fitting using the carrier densities and mobilities from Fig. 3. Dashed lines in (e) are linear-least squares fits.

for the two groups of carriers [Fig. 3 (b)]:

$$S = -\frac{\pi^2}{3}\frac{k_B}{e}k_B T\left[\frac{1}{n(E)}\frac{dn(E)}{dE} + \frac{1}{\mu(E)}\frac{d\mu(E)}{dE}\right]_{E=E_F}.$$

These partial (diagonal) TEPs were then employed in the fitting of the field-dependent Nernst signals to Eq. S2. Figure S9 (a) shows the best fits (solid curves) for N_{cb} ($\mathbf{J_q}\|\mathbf{b}$) at $T = 1.92$ K, 0.52 K, along with the first (dashed) and second (dash-dotted) terms in Eq. S2 of which these fits are comprised. The positive carrier diffusion terms in N_{cb} are opposed by a negative contribution from the product of the Hall conductivity and thermopower (Eq. S2). As noted in the main text and arrow in Fig. 2 (e), this leads to the distinct "kink" in the T dependence of ν/T for $B = 5$ T; the separate terms from the fitting are shown in Fig. S9 (b). The hole and electron partial (off-diagonal) TEPs from the fittings are shown in Fig. S9 (c).

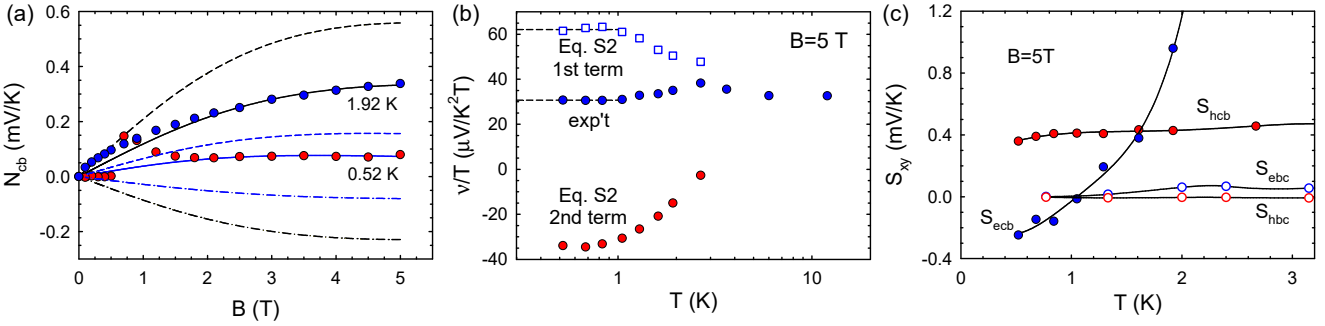

Fig. S9. (a) N_{cb} [from Fig. 2 (a) and Fig. S8 (a)] at $T = 1.92$ K, 0.52 K along with best fits (solid curves) to Eq. S2 and the separate contributions from its first (dashed curves) and second (dash-dotted curves) terms. (b) T dependence of ν/T at $B = 5$ T [from Fig. 2 (e) for $\mathbf{J_q}\|\mathbf{b}$] and the separate terms from Eq. S2 based on the fitting analysis. (c) the partial off-diagonal TEPs determined from the fittings.

Band dispersions from photoemission and band theory, effective masses, Fermi velocities, and mean-free paths

Figure S10 (a) shows the calculated Fermi surface (FS) from Ref. 19 constrained by angle-resolved photoemission spectroscopy (ARPES). As mentioned in the main text, rather unique k_c dispersions caused by hybridization through long-range indirect hopping to the gapped xz and yz valence and conduction bands are responsible for the small Fermi surface (FS) warping (appearing as "fingers" in the upper sheet (red) near $k_c c/2\pi = 0.25, 0.75$ and the bulge in the lower sheet (blue) at $k_c c/2\pi = 0.5$). These dispersions and the associated FS warping are sensitive to the position of E_F and thus to the Li stoichiometry assumed in the calculations (see, e.g., Fig. 13 in Ref. 19). The k_c dispersions at $k_b b/2\pi = 0.25$ shown in Fig. S10 (b) were employed in generating the approximate reconstructed FS of Fig. 3 (d) and (e), and thus do not incorporate changes in the dispersions with energy. The spin-density wave gapped bands (and their spin splitting) [Fig. S10 (c)] are depicted for $\Delta_{SDW} \simeq 65$ meV [19]. We see that the hole pockets form from the lower of the gapped upper sheet (red) and the electron pocket from the upper of the gapped lower sheet (blue).

Effective masses, $(m^*)^{-1} = (1/\hbar^2)\partial^2 E/\partial k^2$ and Fermi velocities, $v_F = (1/\hbar)\partial E/\partial k$, were computed (Table S1) for electrons (e) and holes (h) along k_c at $k_c c/2\pi = 0.25$ and $k_c c/2\pi = 0.5$ for the upper (red) and lower (blue) bands, respectively, of Fig. S10 (b), and along k_b at the top (red) and bottom (blue) of the bands in Fig. S10 (c).

Table S1. Effective masses and Fermi velocities computed from Fig. S10.

carrier type	$m^*(m_e)$	$v_F(10^5\mathrm{m/s})$
in-chain electrons (eb)	0.016	1.80
interchain holes (hc)	0.97	0.20
in-chain holes (hb)	0.016	1.80
interchain electrons (ec)	2.70	0.14

Mean-free paths for each carrier group for SC samples were computed (Fig. S11) from the mobilities and parameters in Table S1: (1) $\ell = (\mu/e)m^* v_F$ appropriate for $T < T_F \sim 18$ K, and (2) $\ell = (\mu/e)m^* v_{th}$ where $v_{th} = \sqrt{2k_B T/m^*}$ is the thermal velocity appropriate to nondegenerate electrons (at $T > T_F$).

$T \to 0$ conductivities of the non-superconducting specimens

Figure S12 shows the low-T in-chain and interchain conductivities at $B = 0$ and $B = 5$ T for the non-superconducting specimens. The interchain conductivities extrapolate to zero at finite T (dashed lines), indicating the absence of metallicity.

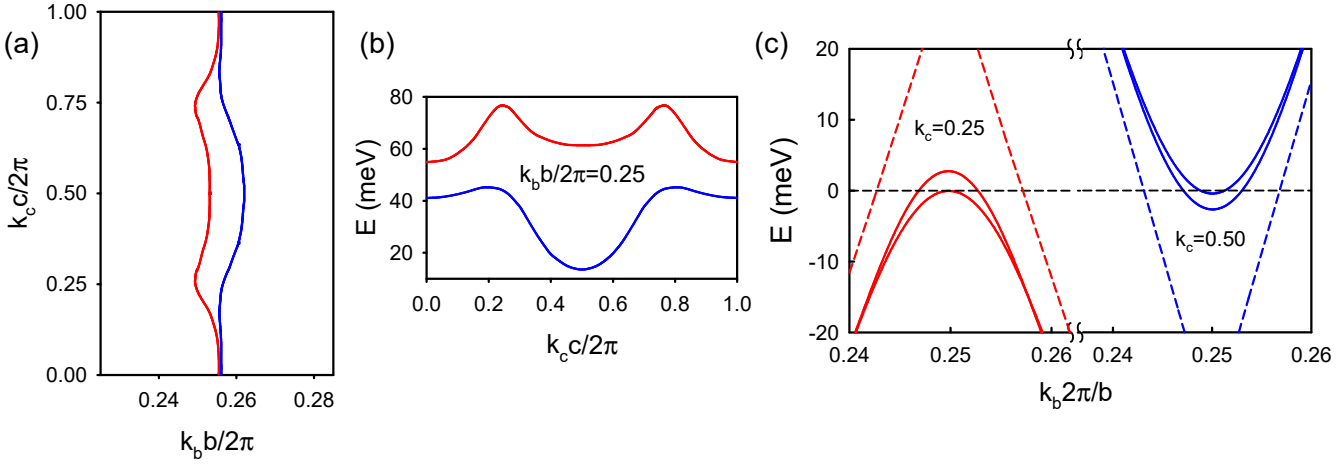

Fig. S10. (a) The unreconstructed Fermi surface from Ref. 19 showing the upper (red) and lower (blue) sheets (note the greatly expanded scale for the k_b axis). (b) k_c dispersions for the two FS sheets at $k_b b/2\pi = 0.25$ (energy is referenced to the center of the band gap between d_{xz} and d_{yz} bands). (c) Unreconstructed k_b dispersions for the upper (red) and lower (blue) FS sheets with their $q_{SDW} = 2k_F$ translations (dashed curves) and the spin-split gapped bands (solid curves) for $\Delta_{SDW} \simeq 65$ meV, adjusted to produce an average $E_F = 1.5$ meV for the majority and minority spin bands as assumed in Fig. 3 (d).

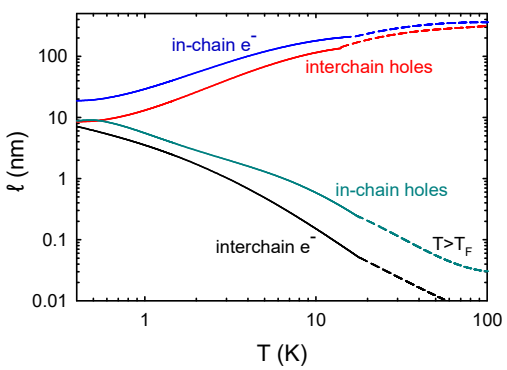

Fig. S11. Mean-free paths for SC samples computed using the carrier mobilities determined from the anisotropic two-band analysis. The effective masses and Fermi velocities from Table S1 were employed at $T < T_F$ (solid curves). Dashed curves for $T > T_F$ use $v_{th} = \sqrt{2k_bT/m^*}$ in place of v_F.

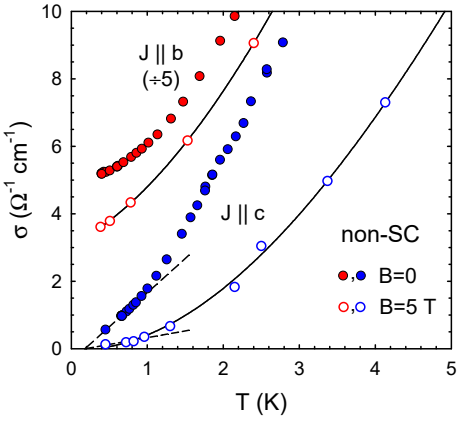

Fig. S12. Low-T conductivities for the non-SC crystals along and transverse to the chains for $B = 0$ (solid symbols) and $B = 5$ T (open symbols). The dashed lines are linear-T extrapolations of the lowest-T data showing the absence of metallicity along the interchain direction.